Burned vegetation recovery trajectory and its driving factors using satellite remote-sensing datasets in the Great Xing'An forest region of Inner Mongolia

Qiyue Zhang[A,B] (iD), Saeid Homayouni[B], Pengwu Zhao[A] and Mei Zhou[A,*]

For full list of author affiliations and
declarations see end of paper

*Correspondence to:
Mei Zhou
Forestry College, Inner Mongolia
Agricultural University, No. 275, East Xin
Jian Street, Hohhot, 010011, China
Email: dxal528@aliyun.com

ABSTRACT

Forest fire is one of the most important factors that alter a forest ecosystem's biogeochemical cycle. Large-scale distributed burned areas lose their original vegetation structure and are more impacted by climate change in the vegetation recovery process, thus making it harder to restore their original vegetation structure. In this study, we used historical Landsat imagery and the LandTrendr algorithm in the Google Earth Engine platform to study and identify post-fire stages in the Great Xing'An Range of Inner Mongolia. Moreover, we categorized different post-fire vegetation recovery trajectories. The usefulness of spectral indices was also evaluated in the study region. We applied the Geodetector model to analyze the driving factors of the burned area vegetation regeneration process. The results show that burn severity and earth–atmosphere hydrological cycle are two main impacting factors in the short term after the fire (e.g. 5–6 years). Other climatical conditions affect vegetation recovery, including prolonged vegetation recovery process, hydrothermal circulation process and topographical conditions, seasonally frozen soil, freeze–thaw processes, and climate events. This study improves understanding of the dynamic successional processes in the burned area and the driving factors. Also, the outcomes can facilitate and support sustainable forest management of the Great Xing'An Range.

Keywords: burned area, driving factors, geodector, Great Xing'An Range, Inner Mongolia, LandTrendr, remote sensing data, vegetation recovery trajectory.

Introduction

Wildfire is considered one of the most severe natural disasters and plays a critical role in terrestrial ecosystems (Artés *et al.* 2019). At the same time, a forest fire is an ecological management tool and a crucial factor in ecosystem evolution (Adelabu *et al.* 2020); however, it has harmful natural and socio-economic impacts at various scales (Chuvieco 2009; Aponte *et al.* 2016). Forest fire also indirectly affects the forest ecosystem by promoting forest degradation. Large-scale fire-related forest degradation results in long-term or permanent changes in vegetation coverage (Siscawati 1998).

Moreover, climate change and climate events accelerate the fire risk in forest ecosystems (San-Miguel-Ayanz *et al.* 2013, 2020; Yang *et al.* 2021). High-latitudinal regions influenced by the amplification of global-warming signals show increased fire activity (Girardin 2007; Marlon *et al.* 2008). Climate change and climate events lead to fuel moisture change, shaping the patterns of future forest fires. Interactions of abiotic and biotic climate-changing processes are more likely to amplify disturbances, with coniferous forest and boreal ecosystems the most affected (Seidl *et al.* 2017). Over recent decades, climate change has significantly affected post-fire forest recovery. Climate change also increases forests' water deficits and climate tolerance.

As the largest boreal forest in China, the Great Xing'An Range has the most vegetation types in the Eurasian boreal biome (Fang *et al.* 2015). Existing research recognises this region's teleconnections between climate events and wildfires (Yao *et al.* 2017). The local

forest ecosystem shows an adaptive trend in growth response to the climatic changes, with trees more susceptible to climate changes than dwarf shrubs (Yang *et al.* 2020), and the Dahurian larch and the Mongolian pine tending to be distributed separately (Li *et al.* 2021a). Moreover, permafrost is widely distributed in the Great Xing'An Range. The permafrost degradation process significantly affects the soil-water balance, eventually changing vegetation distribution (Li *et al.* 2021b). Post-fire forest regeneration experiments indicate that limited artificial promotion can be helpful to local vegetation recovery. However, broadleafed species become the major regenerating species under natural regeneration conditions (Chen *et al.* 2014). Furthermore, annual temperature and spring phenology also show a stronger influence than other climatical conditions (Tang *et al.* 2015; Fu *et al.* 2018). Other researchers state that the duration of daily sunshine in summer is the critical factor in gross primary productivity in the Great Xing'An Range (Hu *et al.* 2018).

Remote sensing imagery and geospatial analysis have historically been the most cost-effective tools to study forest fire (Kourtz 1968; Hawe and Fuquay 1969; McKetta 1969). Cardil *et al.* (2021) recently developed multi-factor models to study forest fire occurrence and burned area vegetation recovery. Many optical spectral indices have been used to examine relationships between remote-sensing data and forest fire (White *et al.* 1996; Thomas Ambadan *et al.* 2020). Landsat time series has long been used in change detection (Kennedy *et al.* 2012; Zhu 2017). Previous research has established many algorithms such as Breaks for Additive Seasonal and Trend (BFAST) (Verbesselt *et al.* 2010), Continuous Monitoring of Forest Disturbance Algorithm (CMFDA) (Zhu *et al.* 2012) and Vegetation Change Tracker (VCT) (Huang *et al.* 2010). LandTrendr is a spectral trajectory-based segmentation algorithm that enables the identification of both short-term events (e.g. wildfire) and long-term changes (e.g. forest degradation). LandTrendr has good performance in many different regions for evaluating the disturbing and recovery process (Kennedy *et al.* 2012; Bright *et al.* 2019; Wang *et al.* 2021; Liu *et al.* 2022). The Google Earth Engine (GEE) platform is a popular and freely available cloud computing service that boosts remote-sensing analyses and provides access to varieties of earth observation products at a planetary scale (Gorelick *et al.* 2017). The combination of LandTrendr and GEE enables fast application and high efficiency of LandTrendr (Kennedy *et al.* 2018).

The Geographical Detector Model (GDM) was initially designed to assess health risk across different geographical strata (Wang *et al.* 2010). Their following studies improved and expanded the GDM in ecological phenomena (Wang *et al.* 2016) and other aspects (Luo *et al.* 2016; Xu *et al.* 2018). Su *et al.* (2020) investigated the driving factors of soil salinisation distribution. Chen *et al.* (2022a) found that slope angle controls permafrost-related seasonal deformation in the Qinghai-Tibet Plateau. To date, several attempts have investigated GDM for analysing vegetation growth. For example, Zhu *et al.* (2020) used GDM to study natural and anthropogenic factors in northeast China. Chen *et al.* (2021) analysed the driving factors of vegetation net primary productivity. Existing research on vegetation dynamics suggests that GDM plays an essential role in analysis of vegetation driving factors (Guo *et al.* 2020; Huo and Sun 2021; Zheng *et al.* 2021).

A considerable amount of literature on post-fire vegetation recovery has been published. Though these works studied a variety of forest ecosystems (Bartels *et al.* 2016; Hao *et al.* 2022), fewer works defined the different succession stages (Meng *et al.* 2015; João *et al.* 2018; Viana-Soto *et al.* 2020), and few have been applied to the Great Xing'An Range (Shi *et al.* 2019; Guo *et al.* 2021). Our study focuses on classifying and identifying vegetation recovery in burned areas at different stages and their driving factors in the Great Xing'An Range. We tried to understand post-fire biodiversity and vegetation composition better and promote knowledge of the boreal ecosystem's resilience to wildfire. We used the modified GEE LandTrendr (Kennedy *et al.* 2018) and GDM (Wang *et al.* 2010) for analysis of Landsat historical data. The main goals are to (1) classify different trajectories of burned area vegetation recovery in two study areas, (2) categorise the differentiation between sustained management region and naturally recovered region, and (3) find the driving factors of each recovery stage.

Methodology

Study areas

Our study region lies in the northern forest of the Great Xing'An Range of Inner Mongolia, located in northeast China (Fig. 1a), which falls at the junction of two provinces: Inner Mongolia and Heilongjiang. Latitude is 50.03–53.33°N, and longitude is 119.49–123.25°E, covering an area of 1654 km^2, most parts being larch forest. The dominant tree species are Xing'an larch, white birch, and Mongolian pine (*Pinus sylvestris* var. *mongolica*) (Wang *et al.* 2017). The region is characterised by a cold temperate continental climate under the influence of alternating monsoons. Based on meteorology data from 1960 to 2018, the multi-year average annual air temperature ranges from -1 to 1°C (Yue *et al.* 2020) at the Gen'he Meteorological Station. The mean annual precipitation is 438 mm. Precipitation is mainly concentrated in summer during June–September, accounting for 73% of the annual total. Between 1960 and 2018, annual precipitation at Gen'he station increased at an average rate of 15.5 mm per decade. This region has an intact community structure with relatively little artificial disturbance. Nevertheless, this area has become one of China's regions with high forest fire risk because wildfires are frequent. Records show that the
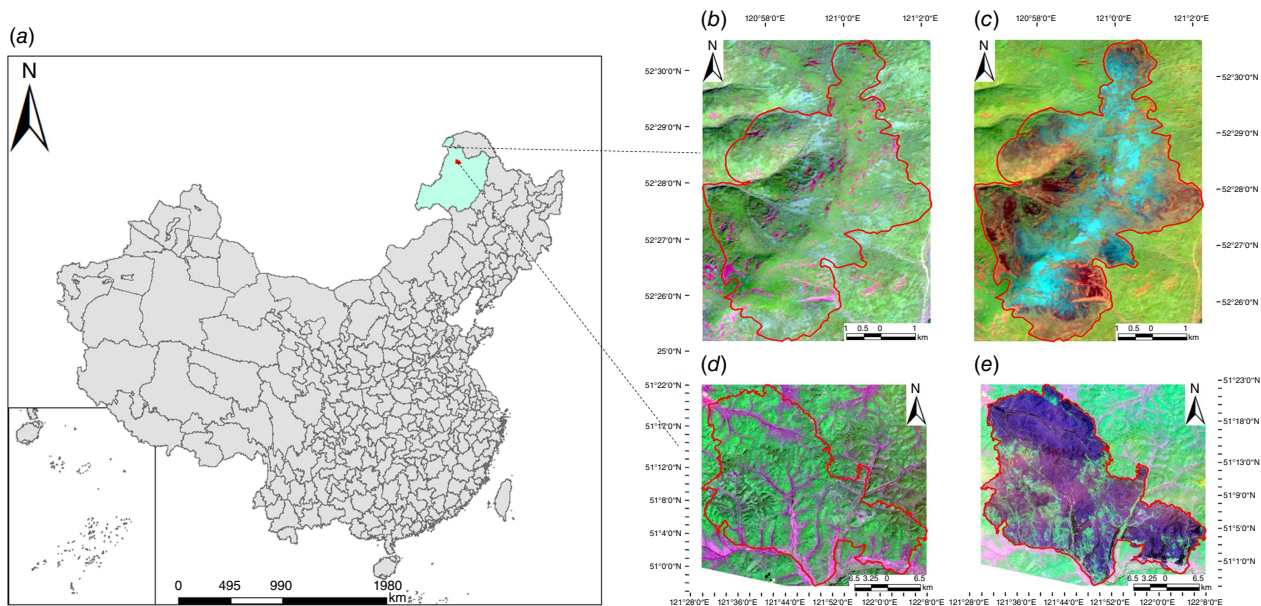
Fig. 1. The study areas in northeast China (*a*); pre- (*b*) and post-fire (*c*) Landsat images (RGB: shortwave infrared, near-infrared, blue) for the northern virgin forest fire (NVF-02) region and pre- (*d*) and post-fire (*e*) Landsat images (RGB: shortwave infrared, near-infrared, blue) of the GenHe fire (GHF-03).

Great Xing'An Range has had over 3400 forest fires in the last six decades (Wang 2020).

Our research was based on two large forest fires in 2002 and 2003. One was the northern virgin forest fire (NVF-02) that occurred on 21 July 2002 and burned 3438.684 ha of forest. The other was the GenHe fire (GHF-03) on 5 May 2003, which burned 104 347.44 ha of forest. These two regions have had no subsequent fires after the primary fire disturbance. The main difference between these two forest fires is that the GHF-03 region was reforested by the local forestry bureau after the fire, while the NVF-02 region naturally recovered.

Data resources

All remote-sensing data in our study were collected from the GEE platform. The Landsat time series images were all chosen from surface reflectance product stores in GEE, including Landsat 5, Landsat 7, and Landsat 8, the GEE ImageCollection IDs for each image collection being LANDSAT/LT05/C02/T1_L2, LANDSAT/LE07/C02/T1_L2, and LANDSAT/LC08/C02/T1_L2, respectively. All Landsat time series images were processed to create the cloud, shadow, water, and snow masks in LandTrendr. A research period of 26 years, from 1995 to 2020, was used. We mainly used the growing season data (20 May to 20 September).

We used the ALOS DSM (Advanced Land Observing Satellite Digital Surface Model) to extract topographic information. The ALOS DSM was created by combing the SRTM CHILI (Shuttle Radar Topography Mission Continuous Heat-Insolation Load Index) and the multi-scale topographic

position, which has a spatial resolution of 30 m (Tadono *et al.* 2014; Takaku *et al.* 2014, 2016; Bhalla *et al.* 2016).

Due to insufficient long-term field investigation images, the validation data of spatial vegetation recovery relied on Landsat time-series historical data, GEE historical data, and the data provided by the local forest bureau.

We acquired nine indices from the Terra Climate dataset (Abatzoglou *et al.* 2018) as climate variables in our study. Terra Climate is a global monthly climate dataset at 0.2 arc min spatial resolution. We divided these nine climate indices into Groups 1 and 2.

Group 1. The climate data for the growing season data were acquired for May–September every year, mainly representing the growing season's impact and vegetation recovery, which contained the Palmer Drought Severity Index (PDSI) and Reference Evapotranspiration (PET) index showing the evaporative demand of soil moisture. Climate Water Deficit (DEF) and Precipitation Accumulation (PR) indices indicated climatic moisture conditions. The Soil Moisture (SOIL) index indicates the soil moisture conditions. The indices of Downward Surface Shortwave Radiation (SRAD) and Minimum Temperature (TMMN) indicated solar radiation.

Group 2. The non-growing season data acquired from October to April of the following year were mainly used to determine if the climatic conditions prior to the growing season affected the vegetation recovery. A former study showed that vegetation is affected by hydrothermal conditions in the permafrost region (Jin *et al.* 2021). The Snow Water Equivalent (SWE) index was used to evaluate the impact of the frozen soil and spring snow depth.

The Maximum Temperature (TMMX) index was used to assess the winter temperature change.

Image processing and statistical analysis

### Spectral indices and LandTrendr parameters

We used the LandTrendr spectral-temporal segmentation algorithm to calculate the spectral indices, delineate burned areas, and derive trajectory metrics of forested pixels. To better understand vegetation recovery tendencies, we needed to choose a vegetation-related index that best correlates with local vegetation recovery. The selected indices are tasselled cap components – tasselled cap wetness, tasselled cap greenness, tasselled cap brightness (Crist 1985), and tasselled cap angle (Powell *et al.* 2010) – they all show a relation to the mixed deciduous and coniferous forest (Dymond *et al.* 2002; Powell *et al.* 2010). We also used the Normalised Difference Vegetation Index (NDVI) (Tucker 1979), Normalised Difference Moisture Index (NDMI) (Jin and Sader 2005), and Normalised Burn Ratio (NBR) (van Wagtendonk *et al.* 2004) indices. The NDVI is widely used to quantify active vegetation, the NDMI is sensitive to canopy structure and leaf water content (Liu 2016), and the NBR is a broadly used vegetation index in burned areas and provides general vegetation growth conditions (Bright *et al.* 2019). In addition, because the near-infrared and shortwave infrared bands show a solid connection to vegetation change (Xiao *et al.* 2002), we also used these two indices in our pre-analysis.

The UI Pixel Time Series Plotter was used to start the pre-study. Root mean square error (RMSE) was used to determine which index performed best. We randomly chose sample plots of burned area for each study region (NVF-02 and GHF-03). Also, another undisturbed region was used in this step to evaluate whether the index was sensitive to vegetation change. Based on the RMSE results (Fig. 2), in all three sample regions (NVF-02, GHF-03, and undisturbed), NBR showed the lowest RMSE and excellent pixel efficiency compared to other indices. We used the NBR as our trajectory classification-based index and NDVI as the pre-fire vegetation condition index to get more accurate and stable results in subsequent analyses.

The core of LandTrendr trajectory segmentation is to eliminate noise but capture both abrupt and slow phenomena in the Landsat time series. This purpose requires LandTrendr to simplify the complex model into the best-fitting simple model iteratively. Therefore, we tested some parameters to help determine the final model (Table 1), and more details of this segmentation process can be found in Kennedy *et al.* (2010).

Vegetation recovery trajectory segmentation and classification

We tried to use the most relevant and stable index from the test we did before in this step. The recovery ratio (RR)
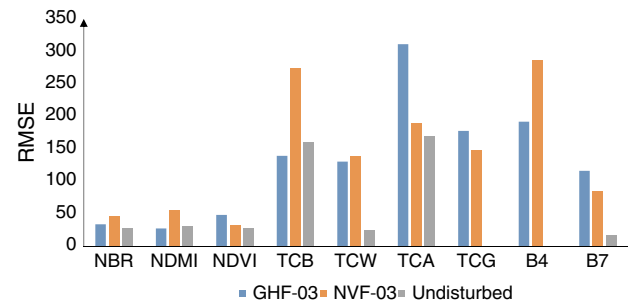
Fig. 2. RMSE results of different indices among northern virgin forest fire (NVF-02), GenHe fire (GHF-03), and undisturbed regions (pre-study indices performance evaluation). Abbreviations: NBR, Normalised Burn Ratio; NDMI, Normalised Difference Moisture Index; NDVI, Normalised Difference Vegetation Index; TCB, tasselled cap brightness; TCW, tasselled cap wetness; TCA, tasselled cap angle; TCG, tasselled cap greenness; B4, near-infrared; B7, shortwave infrared.

Table 1. LandTrendr parameters.

Parameter indices names	Tested values	Final values
Max segments	4, 5, 6	5
Spike threshold	1.0, 0.9, 0.75	0.75
Vertex count overshoot	0, 3	3
Prevent 1-year recovery	True, false	True
Recovery threshold	1, 0.5, 0.25	0.25
P-value threshold	0.05, 0.1, 0.2	0.05

Max segments, the maximum number of segments allowed in the fitting process; Spike threshold, before fitting, spikes are dampened if the spectral value difference between spectral values on either side of the spike is less than 1-despike desawtooth proportion of the spike itself; Vertex count overshoot, the initial regression-based detection of potential; Prevent 1-year recovery, disturbance segments of 1-year duration are considered no-change if their change in spectral value when converted to percent vegetative cover, is less than this threshold; Recovery threshold, if a candidate segment has a recovery rate faster than 1/recovery_threshold (in years), that segment is disallowed and a threshold different segmentation must be used; *P*-value threshold, if best-fitted trajectory's *p*-of-*F* value exceeds this threshold, the entire trajectory is considered no-change. Additionally, we set the best model proportion as 0.75 and minimum observations as 6.

was used to classify the vegetation recovery segmentation. The RR describes the ratio of vegetation change magnitude and duration. From the segmentation:

$$RR = \frac{Mag_X}{Dur_X} \quad (1)$$

where X represents the vegetation change year, and Mag and Dur are the magnitude and duration of vegetation change, respectively.

In this work, we used K-means classification, one of the most popular unsupervised ensemble learning algorithms to cluster and classify the different vegetation recovery

patterns (Gouveia *et al.* 2010). It runs efficiently on an extensive database. The clustering process can be divided into two steps: the first was to cluster the RR in each segment into groups. In this step, we ran the different numbers of classes from 12 to 7 to test if more classes would provide a better result. The second step refers to the idea of Bholowalia and Kumar (2014). The elbow method chooses the optimal classes, which explains the percentage of variance as a function of the number of clusters. In this step, we differentiated the class, those who did not add the variance percentage were classified into the minority classes, and those classes that added the variance percentage were classified into the majority classes. We reduced the classes by combining the minority and majority classes based on distance. The yearly change map was also used to determine if the RR had the same value while the recovery condition differed (i.e. RR is the same when mag = 10 and dur = 5 as when mag = 4 and dur = 2). The yearly change map ensured that classified RR was in the same condition. Each region finally had five classes of recovery categories.

According to the original index-based (NBR-based) vegetation yearly change, vegetation recovery can be divided into three stages based on recovery time (Key and Benson 2006). The pre-fire vegetation indices values are the reference values to assess the vegetation recovery conditions. This judgment is based on the linear regression of different vegetation recovery stages. The trendline of pre-fire showed a steady trend. However, the different post-fire stages had different recovery rates. Fig. 3 shows the NBR-based vegetation recovery trajectories and stages.

Vegetation recovery driving factors

To investigate the vegetation recovery driving factors, we used the GDM to calculate the driving factors of the burned area vegetation recovery. The core of the GDM is stratified spatial heterogeneity (Wang *et al.* 2016). Stratified spatial heterogeneity refers to intra-strata having more geographical attribute similarities than inner-strata, which implies the natural geographical phenomenon by evaluating the association of geographical attributes between regional variances

and the global variance of data (Guo *et al.* 2022). The strata from the definition of statistical in the GDM model thus can correspond to the definition of geographical classes in this study (Wang *et al.* 2010). Due to the climate variables at low resolution compared with Landsat series images, we need to differentiate the spatial resolution of the climate dataset. Previous research (Booij 2002; Masson and Knutti 2011) on climate scale found a good agreement with observations yet retained most regional features of climate signal under 20 km or lower resolution. Former studies proved that different spatial resolution data could be used in the GDM model by applying a rescale method (Zhang *et al.* 2021; Hu *et al.* 2022). Thus we used the Nearest Neighbour method (Danahy *et al.* 2007) to rescale the climate data to match our derived data. The q-value can determine this spatial association:

$$q = 1 - \frac{\sum_{h=1}^{L} N_h \sigma_h^2}{N \sigma^2} \quad (2)$$

where h is the strata ($h = 1, 2, …, L$) of Y or X, N_h and N refer to the number of strata h and whole study region, respectively, and σ_h and σ are the variances of strata h and total strata, respectively. The q-value, within [0, 1], evaluates the association between X and Y: 0 implies no association between dependent and explanatory variables, and 1 suggests that X can perfectly explain the distribution of Y.

The functionality of the factor detector is to assess the coupling degree of X to Y using the q- and P-values. The q-value indicates the spatial association and the P-value refers to the significance. The functionality of the ecological detector implies two explanatory variables that have different impacts on the spatial distribution of Y. Ecological detectors are determined using the F-test value. The interaction detector function reveals whether two explanatory variables interact with the dependent variable. The interaction relationship of GDM is presented in Table 2. In this table, 'Weaken,' 'Independent', and 'Enhance' describe the impact of two explanatory variables' interaction on the dependent variable, while 'Uni', 'Bi', and 'Nonlinear' mark the correlation between this interactive impact and the influence of the two explanatory variables themselves.
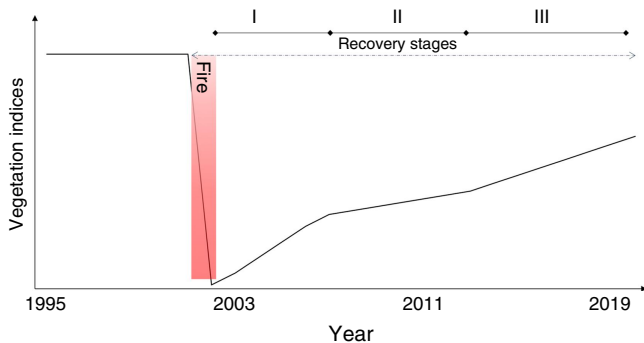

Fig. 3. An example of fitted vegetation recovery trajectories.

Table 2. Interaction between X variables.

Description	Interaction
$q(X1 \cap X2) < \text{Min}(q(X1), q(X2))$	Weaken, nonlinear
$\text{Min}(q(X1), q(X2)) < q(X1 \cap X2) < \text{Max}(q(X1), q(X2))$	Uni-weaken
$q(X1 \cap X2) > \text{Max}(q(X1), q(X2))$	Bi-enhance
$q(X1 \cap X2) = q(X1) + q(X2)$	Independent
$q(X1 \cap X2) > q(X1) + q(X2)$	Nonlinear enhance

The Geodetector package (Song 2018) in R Studio is an analysing tool developed to apply the GDM function and get the spatial stratified heterogeneity result. Details about the Geodetector package can be found on the official website (Xu and Wang 2016). To better understand the association of fire severity, pre-fire conditions, and topographic and climatic conditions in the vegetation recovery process, we used 14 variables to explore this association, which were acquired and derived from the Landsat series and other data introduced before. All variables are shown in Table 3. All descriptive data should be under a discrete treatment, stratifying the continuous numerical variable into categorical variables. Because the climate variables are low resolution compared with Landsat series images, we need to differentiate the spatial resolution of the climate dataset. Previous research (Booij 2002; Masson and Knutti 2011) on climate scale found good agreement with observations, yet retained most regional features of climate signal at 20 km or lower resolution. Climate data also have at least five pixels in each study region, meeting the requirement of the GDM model.

Hence, we consider the climate data as naturally heterologous distributed categorical variables rather than rescale them. In this step, we classify all needed variables in ArcGIS.

Evidence shows a strong relationship between fire severity and vegetation recovery of burned areas (Jin *et al.* 2012). Most likely, it represents the function of fire in the altered forest ecosystem. We evaluated fire severity by classifying dNBR values and the rules based on the USGS classification table (Key and Benson 2006). Severely burned areas are where most vegetation is burned to death. In moderately burned areas, nearly half of the vegetation is burned. Finally, the mild class is those under little or no influence. The dNBR are calculated from NBR:

$$NBR = \frac{nir - swir}{swir - nir} \quad (3)$$
$$dNBR = NBR_{before} - NBR_{after} \quad (4)$$

We used NDVI for pre-fire vegetation conditions. The NDVI values used the Jenks natural breaks classification

Table 3. Driving factor analysis list.

Variables		Units	Description
Dependent variable	Recovery Ratio (RR-NBR)	Z-values	Represents the slope of vegetation trajectory at each segment
Independent variables			
Pre-fire conditions	NDVI$_{00-02}$	Values from −1 to 1	Shows the pre-fire conditions, and NDVI represents the vegetation cover (five classes)
Fire severity	dNBR (differenced Normalised Burn Ratio)	Values from −1 to 1	Burned area severity classification is based on the USGS (Key and Benson 2006)
			Enhanced regrowth: dNBR < −0.1
			Unburned: −0.1 ≤ dNBR < 0.1
			Low severity: 0.1 ≤ dNBR < 0.27
			Moderated-low severity: 0.27 ≤ dNBR < 0.44
			Moderate-high severity: 0.44 ≤ dNBR < 0.66
			High severity: dNBR ≥ 0.66
Topography	DEM (digital elevation model)	m	50 m interval
	Slope	From 0° to 90°	Plain (0–0.5°), valley (0.5–2°), lower slope (2–5°), slope (5–15°), upper slope (15–35°), cliff (35–55°), ridge (55–90°)
	Aspect	Values from 0° to 360°	North (337.5–360° and 0–22.5°), northwest (292.5–337.5°), northeast (22.5–67.5°), west (247.5–292.5°), east (67.5–112.5°), southwest (202.5–247.5°), southeast (112.5–157.5°), south (157.5–202.5°)
Climatic conditions	DEF	mm	Climate water deficit derived using a one-dimensional soil water balance model
	PDSI	mm	Palmer Drought Severity Index
	PR	mm	Precipitation accumulation
	PET	mm	Reference evapotranspiration (ASCE Penman–Monteith)
	Soil	mm	Soil moisture derived using a one-dimensional soil water balance model
	SRAD	W/m^2	Downward surface shortwave radiation
	SWE	mm	Snow water equivalent derived using a one-dimensional soil water balance model (non-growing season)
	TMMN	°C	Minimum temperature
	TMMX	°C	Maximum temperature (non-growing season)

to build nine NDVI value groups of the NDVI values (Jenks 1967):

$$NDVI = \frac{NIR - RED}{NIR + RED} \tag{5}$$

Topographic conditions were derived from ALOS DSM. The elevations were classified using a 50 m interval. This way, the NVF-02 region has 12 categories, and the GHF-03 region has 13 categories. The slope classification was done using the Guide to Medium-Scale Geomorphological Mapping (Demek and Embleton 1978). To this end, different slope classes were classified into seven classes (Table 3). The aspect was classified into nine classes (Table 3). Moreover, all the climatic conditions used original values as the categorical variables because of their spatial resolution.

Vegetation recovery assessment

A stratified validation based on the recovery categories was performed to evaluate the recovery conditions. Based on the recovery pixel counts, we classified the trajectories of different study regions into five time periods: 2005–2006 (2–3 years post-fire), 2008–2009 (5–7 years post-fire), 2011 (8–9 years post-fire), 2013–2014 (10–13 years post-fire), and 2020 (17–18 years post-fire). Likewise, our validation data were also divided into three parts: investigation data given by the local forest bureau were for the years 2006 and 2014; images from GEE historical images were for 2005, 2011, 2013–2014, and 2020; and the Landsat series provided images of 2008–2009. Other reference images helped to identify the pre-fire conditions (represented by NBR value), and dNBR were also obtained from the Landsat series in the years 2000–2001 and 2003. Note that due to the resolution, we used the NBR value to represent the vegetation coverage of Landsat images (Bright *et al.* 2019).

We randomly established 100 sample plots (30 m × 30 m) of each class in each region to the derived recovery trajectories. A total of 1000 sample plots were then established in the two areas. Six corresponding images were selected for each sample plot, including one pre-fire and five post-fire images. The basis of judgment differed from the data source. The Landsat-derived image defined the NBR value as over 80% of the pre-fire NBR value as recovered (Pickell *et al.* 2016). The GEE historical data were defined as at least 60% of areas covered with vegetation as recovered pixels (Zhao *et al.* 2016). The investigation data were also decided by the vegetation coverage of over 60%. Four criteria were used to evaluate the classification accuracy: global (Overall Accuracy and Kappa Coefficient of Agreement) and per-class measures. The analysis and validation methods are illustrated in Fig. 4.

Results

Post-fire vegetation recovery classification

The charts in Fig. 4 demonstrate the fitted trajectories of the different regions from NDVI, NDMI, and NBR. Although six graphs show an increasing trend in post-fire vegetation recovery, the two regions show dissimilitude. All results showed that the vegetation altered severely after a specific disturbance (fire). All three indices had stability in pre-fire vegetation without much alteration before the fire. There was a slight decrease before the fire, possibly because of vegetation self-restoration and climatic change. Since the vegetation structure had not changed, the values of NBR-fitted trajectories were stable. The NVF-02 region had more abrupt changes than the GHF-03 region, yet the GHF-03 slope change could be divided into three stages and that of NVF-02 into two. The NDMI had a more significant slope in vegetation recovery
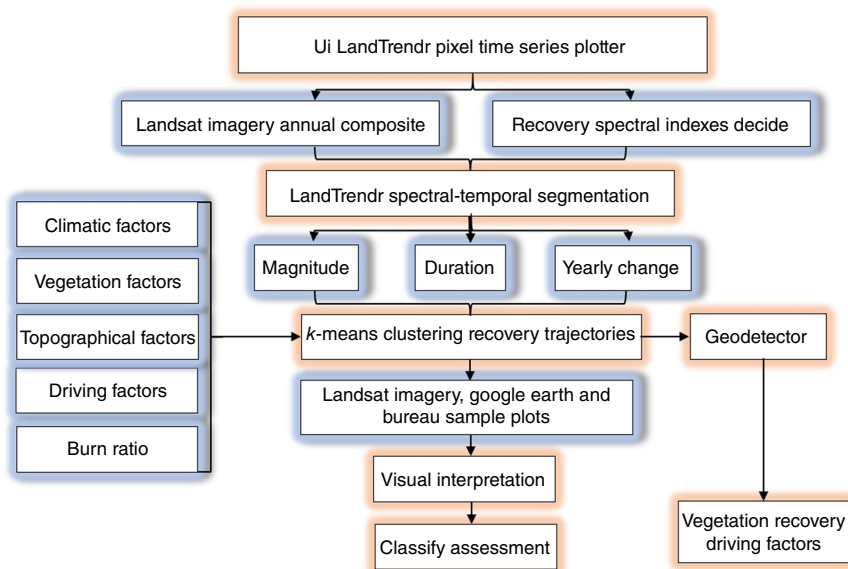

Fig. 4. An overview of the proposed methodology.

trajectories among all three indices, as vegetation correlates more with moisture. As time progressed, the mean values of all three indices in both regions reached the pre-fire value.

Among all fitted trajectories, vegetation recovery could be divided into three stages: short-term high-speed increasing recovery, increasing mid-term recovery, and long-term slow increasing recovery (Fig. 3). Also, of all the graphics shown in Fig. 5, NDMI shows the best fitness result, and NBR shows the worst. All three indices show great fitness. Considering the fitness and classification, we opted for NBR as the trajectory classification index.

We constructed graphics to monitor the vegetation recovery change in each year (Figs 6, 7), so we could better understand the vegetation recovery. The two study regions differed in post-fire management. Each burned area showed the same situation as in the early years after the fire, and the vegetation had a rising trend for 2 years. However, GHF-03 had a rising trend of vegetation recovery immediately following the forest fire. The recovery slowed in the next 2 years, while the vegetation recovery boost for NVF-02 happened 1 year after the fire. This is likely mainly due to terrain factors, as the NVF-02 has a small area with steep hills, and GHF-03 has a large area with few steep hills.

Because this research mainly used remote-sensing data, we analysed the recovery based on its optical characteristics. Our field surveys indicate that fire ash fertilised the post-fire region, and the fire activated seeds under the soil; the rising trend of vegetation mainly consisted of bushes and grasses, and the seeds of trees were activated.

Nearly no pixels occurred in the NVF-02 region after 2009 (Fig. 7). Still, in the GHF-03 region, some vegetation recovery pixels existed after 2009 (Fig. 6). This phenomenon indicates that artificial reforestation could increase burned area vegetation recovery after natural recovery was stable.

We finally classified seven categories of vegetation recovery trajectory (Table 4). The GHF-03 contained five categories: PDSR, CRSC, CR, STRS, and NCR. The NVF-02 also had five categories: LTR, CRSC, CR, MTCR, and NCR.

A solid spatial effect existed on the recovery categories owing to its spatial distribution. Likewise, the two study areas showed a different clustering trend under different magnitudes and change duration (Figs 8, 9).
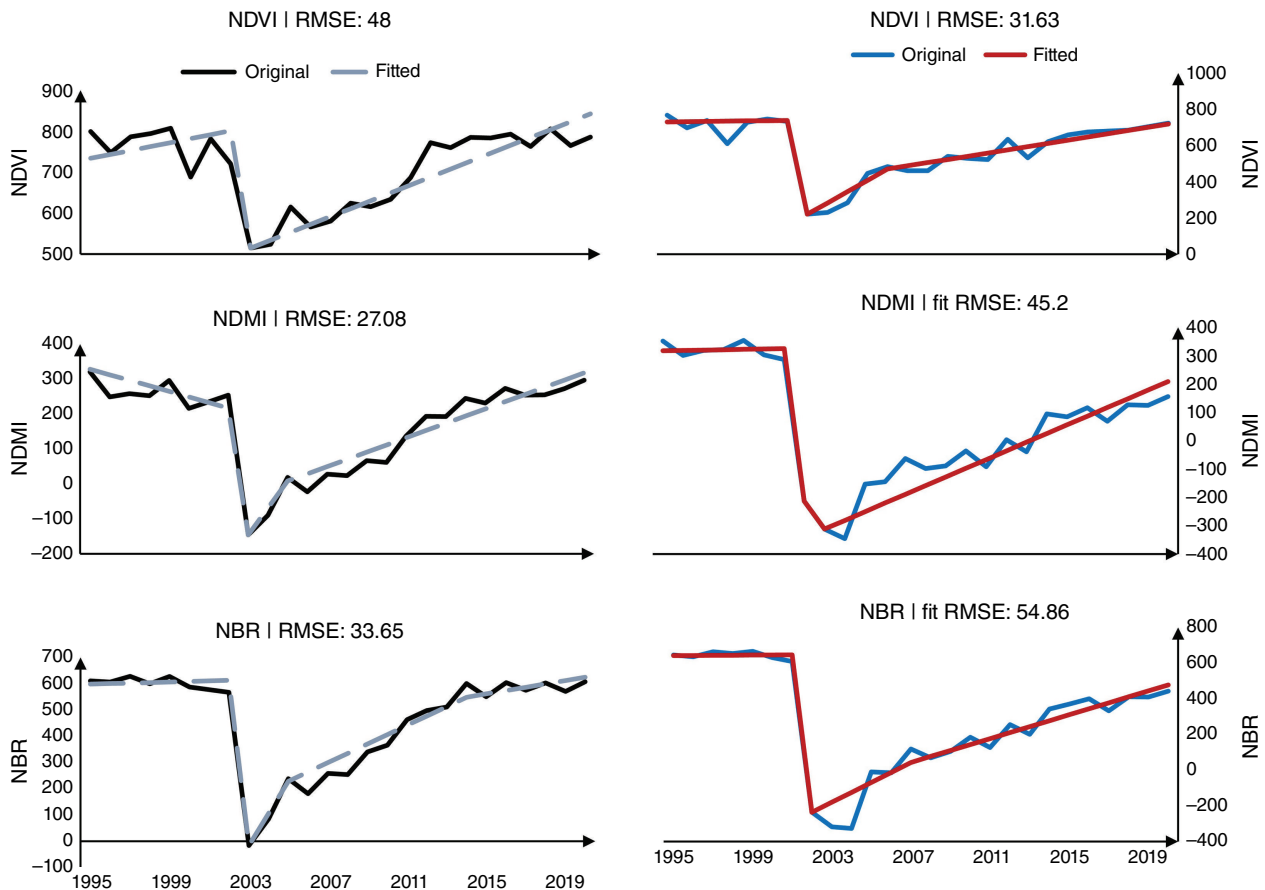

Fig. 5. Different indices-based fitted vegetation recovery trajectories where root mean square error (RMSE) evaluates performance (GHF-03 is left, and NVF-02 is right). Abbreviations: NDVI, Normalised Difference Vegetation Index; NDMI, Normalised Difference Moisture Index; NBR, Normalised Burn Ratio.
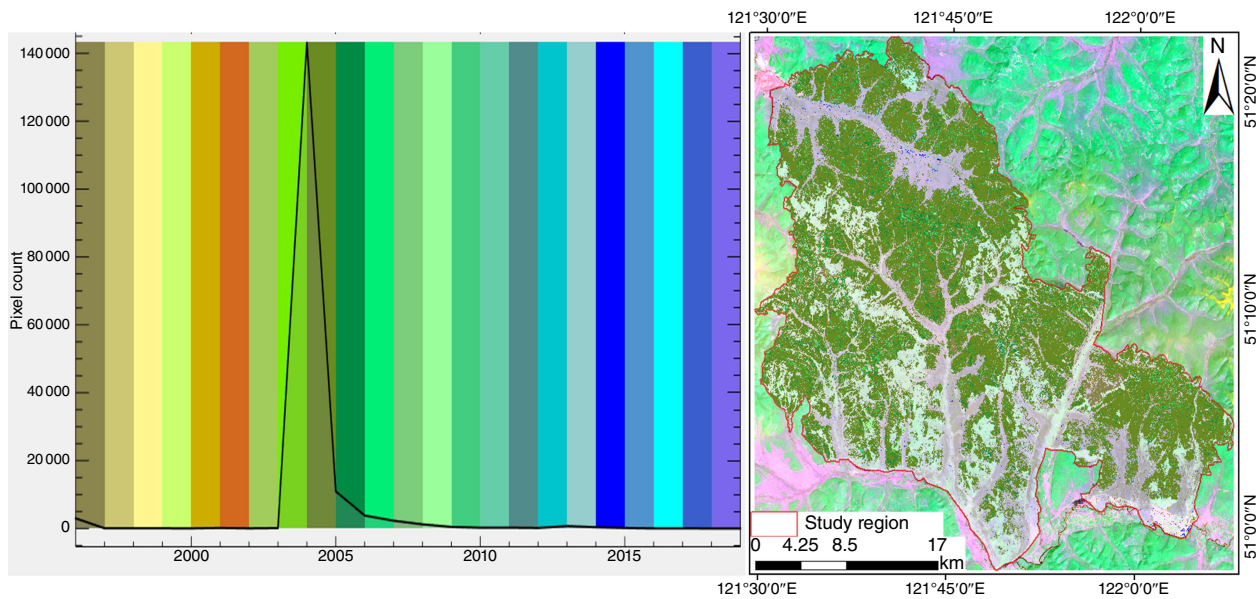
Fig. 6. The pixel counts in different recovery years for the GHF-03 region (the colour bar in the left line chart corresponds to the pixels' colour in the right map).
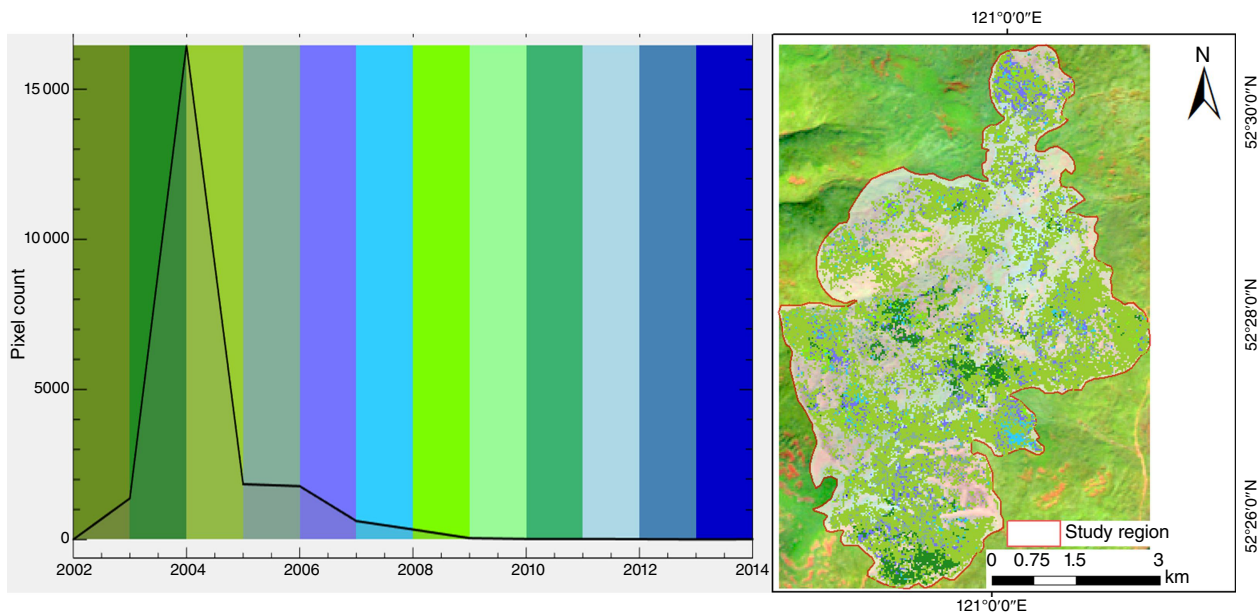
Fig. 7. The pixel counts in different recovery years for the NVF-02 region (the colour bar in the left line chart corresponds to the pixels' colour in the right map).

In GHF-03, vegetation presented a steadier tendency and continuous recovery areas (Fig. 8). The NVF-02 showed more varied recovery categories and more discontinuous recovery areas (Fig. 9). The NCR of each region tended to cluster, possibly because NCR was distributed in fluctuating areas. Different vegetation recovery periods (short-, mid-, and long-term) depended primarily on their relation with seasonally frozen soil. Other locations coupling with the

freeze–thaw process may lead to vegetation growth differences, thus restricting vegetation growth.

Driving factors of different regeneration types

Figs 10, 11 show that no factor had a solid correlation with vegetation recovery, meaning local vegetation had a complex structure. Its recovery was the result of multiple factors

Table 4. Recovery category details.

| Recovery category	Acronym and category	Description
Pre-dominant stable recovery	PDSR (GHF-03)	Pixels show stable vegetation growth before and after the fire.
Continuous recovery with slope change	CRSC (GHF-03 and NVF-02)	Pixels show an increase after the fire but their slope changes.
Continuous recovery	CR (GHF-03 and NVF-02)	Pixels show a continuous increase after the fire.
Short-term recovery stable	STRS (GHF-03)	Pixels show vegetation recovery is extremely slow 5–7 years after the fire.
Non-continuous recovery	NCR (GHF-03 and NVF-02)	Recovery randomly starts or stops within the whole post-fire period.
Long-term recovery	LTR (NVF-02)	Pixels show slow vegetation recovery or stopped 13 or more years after the fire.
Mid-term continuous recovery	MTCR (NVF-02)	Pixels show slow vegetation recovery or stopped 10–13 years after the fire.
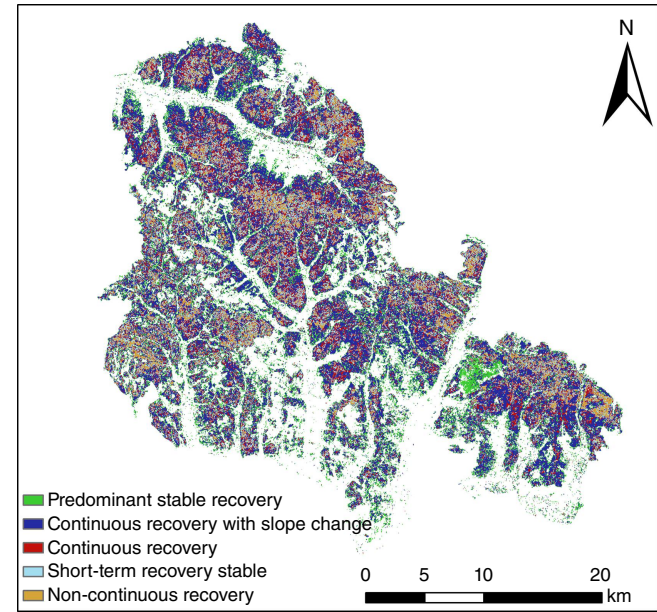
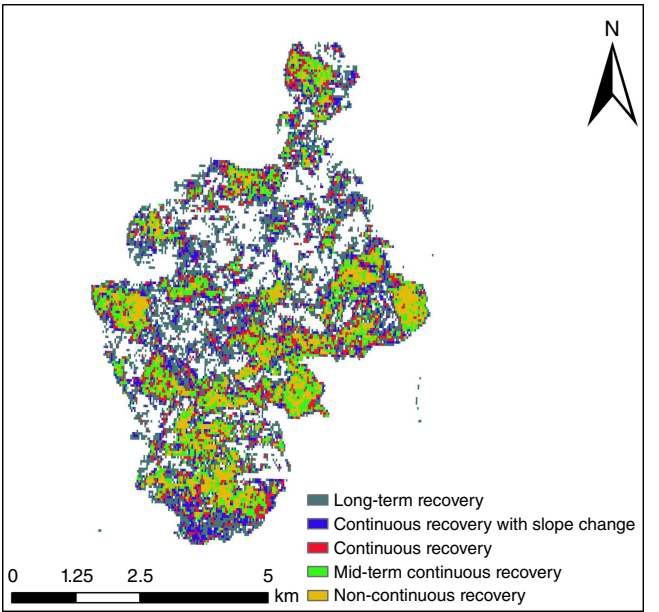**Fig. 8.** LandTrendr-derived vegetation recovery trajectories in GHF-03 burned area region.

Fig. 9. LandTrendr-derived vegetation recovery trajectories in NVF-02 burned area region.

working together. However, different stages showed different correlation results. The factors in stage I had more correlations than in stage II, suggesting that 5–6 years after the fire, vegetation recovery was more easily altered by natural factors.

Among all post-fire stages, the burn ratio (i.e. dNBR) correlated with vegetation recovery more than the pre-fire conditions (i.e. NDVI), implying that some fire-activated species may have changed the original vegetation structure. Regarding topographic factors, in both study regions, the *q*-value and *P*-value indicated that vegetation recovery was slightly correlated with the slope, owing to local pine and larch being primarily located in foothills on a gentle slope. Aspect had relatively little influence, partly because the semi-shady slopes (northwest and northeast) had lower evaporation rates. The DEM had more influence among three topographic conditions, indicating that topography affected vegetation recovery and that the influence of topographic factors on vegetation was relatively long.

Moreover, we compared nine climatic conditions correlated with vegetation recovery (Figs 10, 11). In GHF-03, for stages, I–III, the most influential factor combination changed from the DEF, SOIL, and PET to the combination of SOIL, SRAD, PET, and TMMN. In other words, climatic moisture is key to burned area vegetation growth, which is also an excellent choice when studying climatic change. The factor combination change showed that short-term vegetation recovery was mostly restricted by climatic moisture and soil moisture. The long-term vegetation recovery was affected by multiple factors: growing season temperature, radiance, and moisture. A similar situation was also found in NVF-02.

Interestingly, most factors had a declining trend in stage II in both study regions (Figs 10, 11). This may be caused by the periodic climatic events (i.e. regional drought and Arctic oscillation) that influence northeast China (Center 2020). We also tested the non-growing season
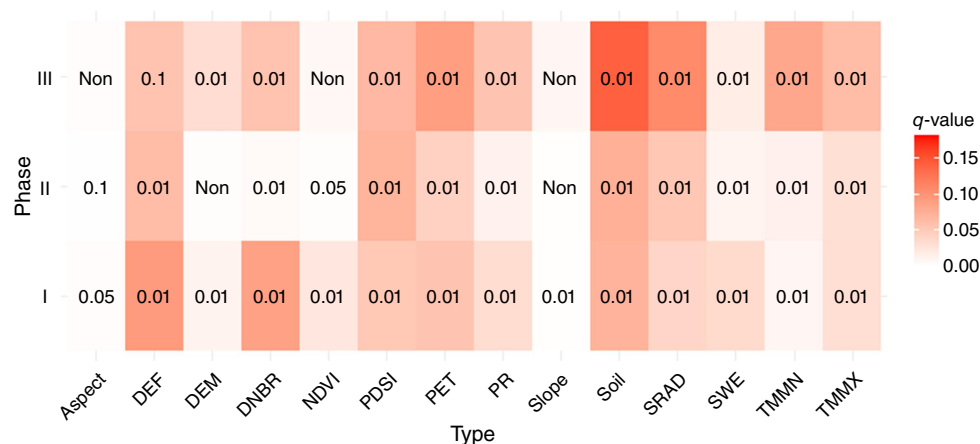
Fig. 10. Factor detector result of GHF-03 region (value in each box is *P*-value which indicates the significance, the colour in each box represents the association between vegetation recovery and listed indices). Abbreviations: DEF, climate water deficit; DEM, digital elevation model; DNBR, differenced Normalised Burn Ratio; NDVI, Normalised Difference Vegetation Index; PDSI, Palmer Drought Severity Index; PET, reference evapotranspiration; PR, precipitation accumulation; SRAD, downward surface shortwave radiation; SWE, snow water equivalent; TMMN, minimum temperature; TMMX, maximum temperature.
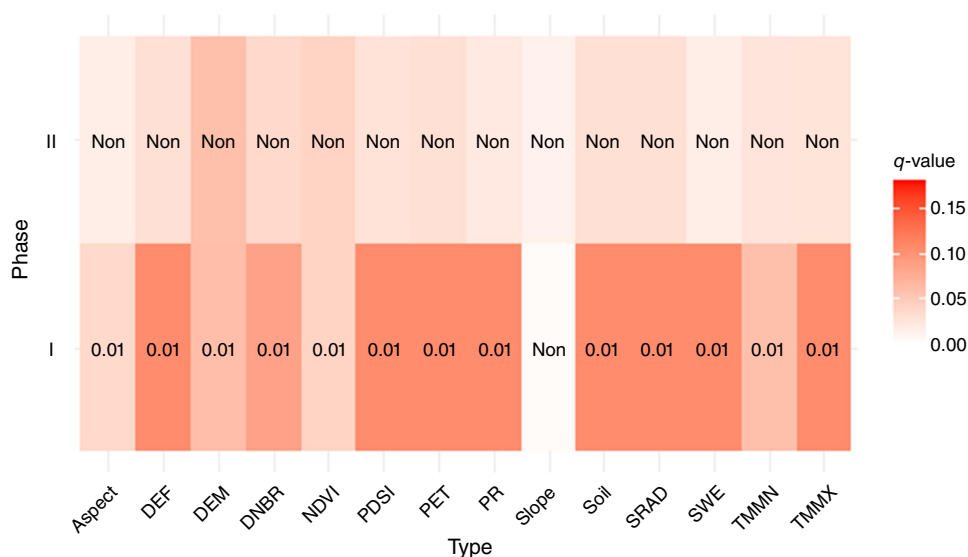

Fig. 11. Factor detector results of NVF-02 region (value in each box is *P*-value, which indicates the significance, the colour in each box represents the association between vegetation recovery and listed indices). See Fig. 10 for definitions of acronyms.

SWE and TMMX due to the location in a seasonal frozen-soil area. The correlation values indicated that seasonal snow and frozen soil's melt–freezing process would also affect the vegetation moisture balance.

The interactive analysis results are graphically shown in Figs 12, 13. Generally speaking, burn ratio and pre-fire vegetation conditions all showed an intense interactive enhanced short-term effect after the fire; this effect decreased with time, possibly because the ashes of the fire accelerated the growth of the first generation of vegetation (mainly bushes and grasses). Topography showed an increasing trend of interactive effects in both regions,

especially NVF-02. The result indicated that the effect of topographic factors on vegetation recovery might need a long time. Aspect and dNBR showed a nonlinear enhancement in both regions in Stage I. Due to the high burn ratio areas, fire most changed the vegetation structure, and the regrowth process was related to the left fertiliser from the fire; ashes most likely stayed in the plain areas compared to steep slopes. The interactive effect of topographic factors was small in GHF-03, and climatic factors were contrary. Regarding the character of each region, we conclude that the enhancement had a temporal-limit trend in GHF-03. There was no interactive enhancement that continued in
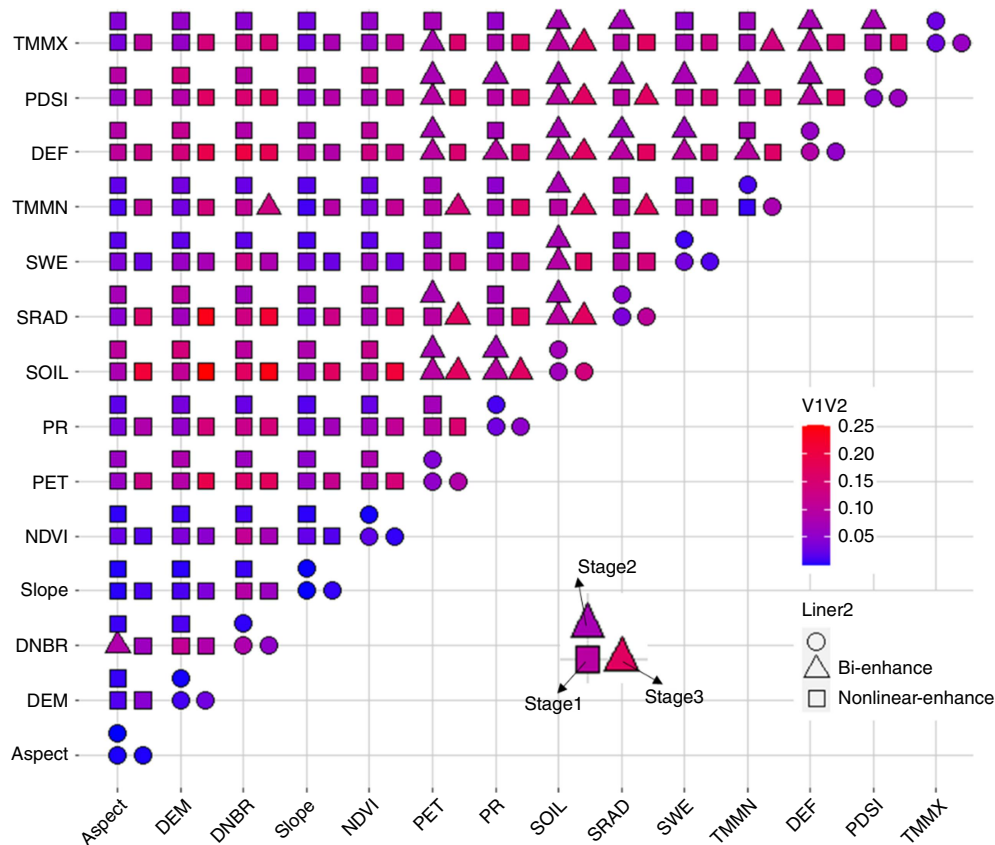
Fig. 12. Interaction detector results for the GHF-03 region (association between vegetation recovery and interaction of two indices). Abbreviations: TMMX, maximum temperature; PDSI, Palmer Drought Severity Index; DEF, climate water deficit; TMMN, minimum temperature; SWE, snow water equivalent; SRAD, downward surface shortwave radiation; SOIL, soil moisture; PR, precipitation accumulation; PET, reference evapotranspiration; NDVI, Normalised Difference Vegetation Index; DNBR, differenced Normalised Burn Ratio; DEM, digital elevation model.

the three stages. Climatic factors showed a significantly enhanced effect with other factors, primarily soil moisture and precipitation.

Recovery accuracy assessment

Both study regions showed great accuracy in most vegetation recovery categories (Table 5). Compared with a previous study (Viana-Soto *et al.* 2020), overall accuracy and kappa coefficient were high. Results for NVF-02 were more accurate, with lower commission and omission errors. The commission and omission errors were more stable in NVF-02 than in GHF-03. These results indicated that the structure of the NVF-02 vegetation recovery was relatively more stable. The continuous recovery classes had higher accuracy than the non-continuous ones. The NCR demonstrated more omission errors among all classes. This may due to the systematic error of chosen sample plots. We could not find a non-continuous recovery region under exactly the same recovery and non-recovery years, which could lead to this type of error.

Discussion

Post-fire trajectory classification

It was not easy to map all burned areas' vegetation regeneration status. It was also a great challenge to classify the vegetation recovery categories because post-fire vegetation recovery is a complex dynamic process impacted by multiple factors. Therefore, we combined historical remote-sensing data with GIS technology to quantify the post-fire vegetation recovery. Because spectral value change is related to vegetation change, we applied NBR recovery ratios at different stages in two Great Xing'An Range burned areas.

We used the LandTrendr algorithm to extract time-series Landsat data and analysed and categorised burned area vegetation recovery trends. The LandTrendr-derived categories enabled us to find slight and recovery time changes, which is essential to understand a long period of forest post-fire vegetation change. The temporal and continuous changes we mapped are vital to reveal vegetation structure change and link with other influencing factors throughout
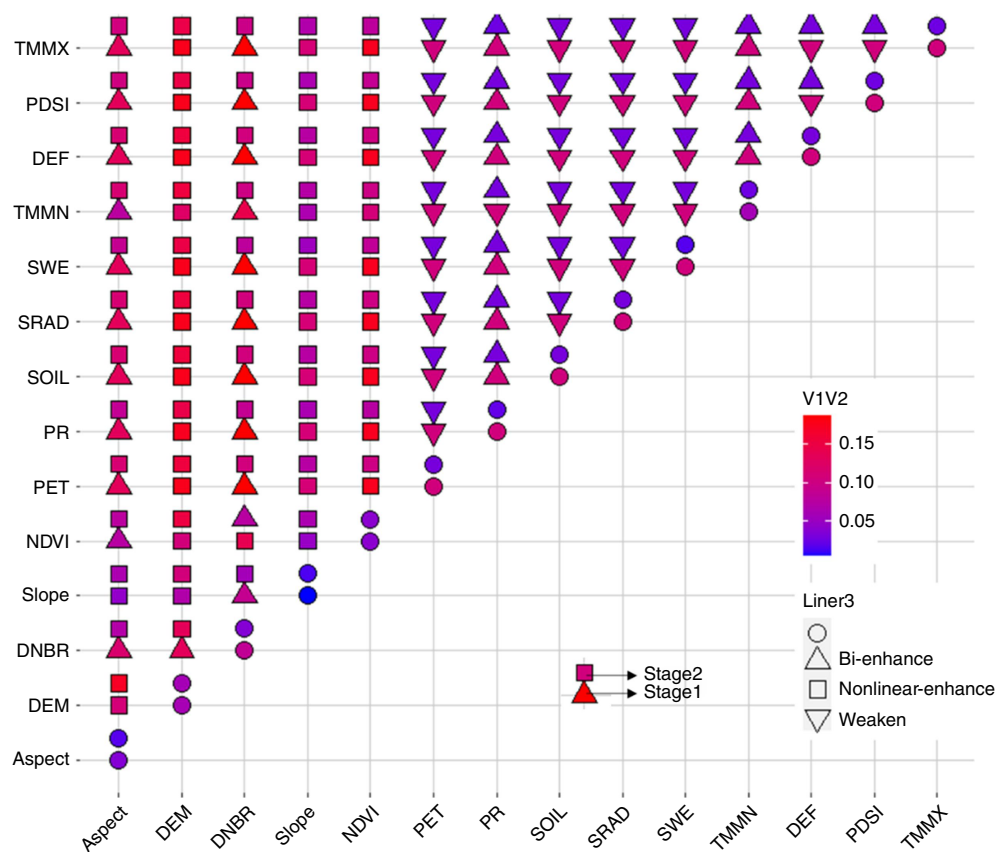
Fig. 13. Interaction detector result for the NVF-02 region (association between vegetation recovery and interaction of two indices). See Fig. 12 for definitions of acronyms.

Table 5. Confusion matrix of estimation (%).

NVF-02	Commission	Omission	GHF-03	Commission	Omission
LTR	8.45	5.77	PDSR	19	10.95
CRSC	5.32	3.5	CRSC	20	1.23
CR	6.22	3.75	CR	8	8.91
MTCR	7.08	4.83	STRS	11	8.45
NCR	5.79	6	NCR	7	17.76
Total	Overall accuracy	Kappa coefficient		Overall accuracy	Kappa coefficient
	93.53	0.92		87.00	0.84

See Table 4 for definitions of acronyms.

the slow vegetation recovery process. Recent studies also analysed the vegetation change process: Viana-Soto *et al.* (2020), using Landsat time-series images, measured post-fire recovery levels in Mediterranean pine forests, and Liu and Lu (2020) detected landscape pattern change in Hulunbeir forest–steppe ecotone. Our finding emphasised the importance of classifying vegetation recovery patterns and promoted understanding of post-fire vegetation change.

The NBR proved to be a stable index of the vegetation change process. Other researchers have had similar results: Reygadas Langarica *et al.* (2020) used LandTrendr-NBR to study forest disturbances in southwestern Amazon forests, and Bonney *et al.* (2020) quantified an analysis of post-fire recovery in Australia. In our region, NBR is suitable for tracking the post-fire vegetation growth and its structure conditions.

A recovery ratio with yearly change detection is a potential method to derive vegetation change. Our research demonstrated that vegetation recovery rates rapidly increased after the fire and declined in later stages. This is likely

because forest fire activated certain seeds and nourished therophytes (i.e. grasses and shrubs). The lower increase rates in Stages II and III are related to the relatively slow perennial plant (i.e. forest) regrowth process. Since the early post-fire stage vegetation structure had already formed, this may have affected the satellite-based observation results. Another reason is that vegetation biomass cannot be precisely measured due to the limitations of optical remote-sensing data (Beamish et al. 2020; Frappart et al. 2020).

A well-known criticism of accuracy assessment is the lack of historical references for high-resolution image data. Therefore, we used visual interpretation to classify our reference data into vegetation and non-vegetation areas. All interpreted classes showed relatively high accuracy. We also found that the NCR class showed a relatively high omission error in both regions. Insufficient cloud-free high-quality images may cause this error in our study regions throughout the research period. As a result, our sample plots did not have the same recovery break time (i.e. every sample plot recovery from 2003 to 2005 stopped in 2006–2008 and restarted for 2009–2012). This combination of findings supports the conceptual premise that LandTrendr allowed us to quantitatively analyse the spatial–temporal dynamics of vegetation recovery in burned areas with acceptable precision. Furthermore, this will increase the understanding of wildfire-induced hydrothermal change and, thus, climate change.

Driving factors of vegetation regeneration

From the results of a spatial stratified heterogeneity regression model, we concluded that the climate is one of the most critical factors influencing post-fire vegetation recovery among topographic factors, fire severity, pre-fire conditions, and climatic factors in the Great Xing'An Range. Of all the climatic conditions, the earth–atmosphere hydrological cycle is vital to burned area short-term vegetation growth, and vegetation growth increases benefits from a positive water balance. Long-term vegetation recovery should consider the whole hydrothermal circulation process: radiance, temperature, and moisture. This also matches the results of several other researchers (Qiu et al. 2021; Chen et al. 2022b) that indicate that warmth and drought will protractedly impact vegetation regeneration.

In this study, we also explored the non-growing season hydrothermal circulation. The seasonal frozen soil's melt–freezing process would slightly impact vegetation recovery, as Zhang et al. (2018) found. We also found that some climate events may influence the climatic impact levels, as noted in Rupp et al. (2000) and Ying et al. (2020).

Topographic conditions show a slow and stable influence on vegetation recovery. The effects tend to couple with other factors like climatic variables. Lee et al. (2018) and Viana-Soto et al. (2020) mentioned topographic factors, especially elevation effect on burned severity, which supports our

result on interactive influence with topographic variables. Moreover, burn severity strongly influenced the short term after the fire, as Viana-Soto et al. (2017) described.

The purpose of this study was to compare two different regions of sustained artificial regeneration and natural recovery. Despite some differences between these two regions, we are convinced that sustained artificial regeneration will promote the recovery of burned area vegetation, although slightly and slowly. Several authors have made similar conclusions (Chen et al. 2014; Aponte et al. 2016; Hu et al. 2019; Wittenberg et al. 2020).

Returning to the question posed at the beginning of this study, it is now possible to state that even though the climatic factors were most influential in the burned area vegetation recovery process, those not presented in this paper should also be considered. Our next focus will be on the topographic condition of seeds and the species' competitive process.

Conclusion

Wildfire is an essential component in the climate system and plays a crucial role in evaluating the carbon cycle and sink. By characterising the post-fire vegetation temporal recovery trajectories, LandTrendr enables us better understand vegetation's adaptive strategies and mechanisms for wildfire disturbance. On the other hand, with the background of global climate change, the discovery of post-fire vegetation regeneration can play an important role in addressing the issue of fire regime and fuel conditions change in a fire-prone region. Some attempts have been made to study post-fire vegetation recovery, but few studies have characterised different vegetation recovery patterns in the Great Xing'An Range. Our work presents a classification idea based on NBR's yearly change and its change continuity. Our work on post-fire vegetation regrowth also demonstrates that burn severity and the earth–atmosphere hydrological cycle are essential factors with short-term influence. Concerning the long term, we advise considering the hydrothermal circulation process and topographical conditions.

Great Xing'An is China's largest and best-preserved pristine area and is China's vital Larix gmelinii forestry resource. However, forest fire risk is high, and this region has frequent forest fires. As an essential terrestrial ecosystem, forests are directly affected by surface hydrothermal changes. The occurrence of forest fires will seriously threaten the regional ecological environment. Studying forest fires in the Great Xing'An area can make up for the lack of research in China and quantitatively monitor the restoration of forests after fires. These burned areas will take a long time to develop into mature forests, thus further necessitating studies on fire regimes, structural change of vegetation biotic communities in the burned area, and different species' competitive processes.

References

Abatzoglou JT, Dobrowski SZ, Parks SA, Hegewisch KC (2018) TerraClimate, a high-resolution global dataset of monthly climate and climatic water balance from 1958–2015. *Scientific Data* 5, 170191. doi:10.1038/sdata.2017.191

Adelabu SA, Adepoju KA, Mofokeng OD (2020) Estimation of fire potential index in mountainous protected region using remote sensing. *Geocarto International* 35, 29–46. doi:10.1080/10106049.2018.1499818

Aponte C, de Groot WJ, Wotton BM (2016) Forest fires and climate change: causes, consequences and management options. *International Journal of Wildland Fire* 25, i–ii. doi:10.1071/WFv25n8_FO

Artés T, Oom D, de Rigo D, Durrant TH, Maianti P, Libertà G, San-Miguel-Ayanz J (2019) A global wildfire dataset for the analysis of fire regimes and fire behaviour. *Scientific Data* 6, 296. doi:10.1038/s41597-019-0312-2

Bartels SF, Chen HYH, Wulder MA, White JC (2016) Trends in post-disturbance recovery rates of Canada's forests following wildfire and harvest. *Forest Ecology and Management* 361, 194–207. doi:10.1016/j.foreco.2015.11.015

Beamish A, Raynolds MK, Epstein H, Frost GV, Macander MJ, Bergstedt H, Bartsch A, Kruse S, Miles V, Tanis CM, Heim B, Fuchs M, Chabrillat S, Shevtsova I, Verdonen M, Wagner J (2020) Recent trends and remaining challenges for optical remote sensing of Arctic tundra vegetation: A review and outlook. *Remote Sensing of Environment* 246, 111872. doi:10.1016/j.rse.2020.111872

Bhalla A, Durham RL, Al-Tabaa N, Yeager C (2016) The development and initial psychometric validation of the eHealth readiness scale. *Computers in Human Behavior* 65, 460–467. doi:10.1016/j.chb.2016.09.015

Bholowalia P, Kumar A (2014) EBK-means: A clustering technique based on elbow method and k-means in WSN. *International Journal of Computer Applications* 105, 17–24.

Bonney MT, He Y, Myint SW (2020) Contextualizing the 2019–2020 Kangaroo Island Bushfires: Quantifying Landscape-Level Influences on Past Severity and Recovery with Landsat and Google Earth Engine. *Remote Sensing* 12, 3942. doi:10.3390/rs12233942

Booij MJ (2002) Extreme daily precipitation in Western Europe with climate change at appropriate spatial scales. *International Journal of Climatology* 22, 69–85. doi:10.1002/joc.715

Bright BC, Hudak AT, Kennedy RE, Braaten JD, Henareh Khalyani A (2019) Examining post-fire vegetation recovery with Landsat time series analysis in three western North American forest types. *Fire Ecology* 15, 8. doi:10.1186/s42408-018-0021-9

Cardil A, Monedero S, Schag G, de-Miguel S, Tapia M, Stoof CR, Silva CA, Mohan M, Cardil A, Ramirez J (2021) Fire behavior modeling for operational decision-making. *Current Opinion in Environmental Science & Health* 23, 100291. doi:10.1016/j.coesh.2021.100291

Center CCC (2020) 'Blue Book on Climate Change in China (2020).' (Science Press: Beijing)

Chen W, Moriya K, Sakai T, Koyama L, Cao C (2014) Post-fire forest regeneration under different restoration treatments in the Greater Hinggan Mountain area of China. *Ecological Engineering* 70, 304–311. doi:10.1016/j.ecoleng.2014.06.016

Chen S-t, Guo B, Zhang R, Zang W-q, Wei C-x, Wu H-w, Yang X, Zhen X-y, Li X, Zhang D-f, Han B-m, Zhang H-l (2021) Quantitatively determine the dominant driving factors of the spatial—temporal changes of vegetation npp in the hengduan mountain area during 2000–2015. *Journal of Mountain Science* 18, 427–445. doi:10.1007/s11629-020-6404-9

Chen J, Wu T, Zou D, Liu L, Wu X, Gong W, Zhu X, Li R, Hao J, Hu G, Pang Q, Zhang J, Yang S (2022*a*) Magnitudes and patterns of large-scale permafrost ground deformation revealed by Sentinel-1 InSAR on the central Qinghai-Tibet Plateau. *Remote Sensing of Environment* 268, 112778. doi:10.1016/j.rse.2021.112778

Chen X, Chen W, Xu M (2022*b*) Remote-Sensing Monitoring of Postfire Vegetation Dynamics in the Greater Hinggan Mountain Range Based on Long Time-Series Data: Analysis of the Effects of Six Topographic and Climatic Factors. *Remote Sensing* 14, 2958. doi:10.3390/rs14132958

Chuvieco E (2009) Global Impacts of Fire. In 'Earth Observation of Wildland Fires in Mediterranean Ecosystems'. (Ed. E Chuvieco)

pp. 1–10. (Springer, Berlin, Heidelberg) doi:10.1007/978-3-642-01754-4_1

Crist EP (1985) A TM tasseled cap equivalent transformation for reflectance factor data. *Remote Sensing of Environment* 17, 301–306. doi:10.1016/0034-4257(85)90102-6

Danahy EE, Agaian SS, Panetta KA (2007) Algorithms for the resizing of binary and grayscale images using a logical transform. In 'Image Processing: Algorithms and Systems V. Vol. 6497'. (Eds JT Astola, KO Egiazarian, ER Dougherty) (SPIE) doi:10.1117/12.704477

Demek J, Embleton C (1978) 'Guide to medium-scale geomorphological mapping.' (Schweizerbart Science Publishers: Stuttgart, Germany)

Dymond CC, Mladenoff DJ, Radeloff VC (2002) Phenological differences in Tasseled Cap indices improve deciduous forest classification. *Remote Sensing of Environment* 80, 460–472. doi:10.1016/S0034-4257(01)00324-8

Fang L, Yang J, Zu J, Li G, Zhang J (2015) Quantifying influences and relative importance of fire weather, topography, and vegetation on fire size and fire severity in a Chinese boreal forest landscape. *Forest Ecology and Management* 356, 2–12. doi:10.1016/j.foreco.2015.01.011

Frappart F, Wigneron J-P, Li X, Liu X, Al-Yaari A, Fan L, Wang M, Moisy C, Le Masson E, Aoulad Lafkih Z, Vallé C, Ygorra B, Baghdadi N (2020) Global Monitoring of the Vegetation Dynamics from the Vegetation Optical Depth (VOD): A Review. *Remote Sensing* 12, 2915. doi:10.3390/rs12182915

Fu Y, He HS, Zhao J, Larsen DR, Zhang H, Sunde MG, Duan S (2018) Climate and Spring Phenology Effects on Autumn Phenology in the Greater Khingan Mountains, Northeastern China. *Remote Sensing* 10, 449. doi:10.3390/rs10030449

Girardin MP (2007) Interannual to decadal changes in area burned in Canada from 1781 to 1982 and the relationship to Northern Hemisphere land temperatures. *Global Ecology and Biogeography* 16, 557–566. doi:10.1111/j.1466-8238.2007.00321.x

Gorelick N, Hancher M, Dixon M, Ilyushchenko S, Thau D, Moore R (2017) Google Earth Engine: Planetary-scale geospatial analysis for everyone. *Remote Sensing of Environment* 202, 18–27. doi:10.1016/j.rse.2017.06.031

Gouveia C, DaCamara CC, Trigo RM (2010) Post-fire vegetation recovery in Portugal based on spot/vegetation data. *Natural Hazards and Earth System Sciences* 10, 673–684. doi:10.5194/nhess-10-673-2010

Guo Y, Zhang X, Wang Q, Chen H, Du X, Ma Y (2020) Temporal changes in vegetation around a shale gas development area in a subtropical karst region in southwestern China. *Science of the Total Environment* 701, 134769. doi:10.1016/j.scitotenv.2019.134769

Guo M, Li J, Yu F, Yin S, Huang S, Wen L (2021) Estimation of post-fire vegetation recovery in boreal forests using solar-induced chlorophyll fluorescence (SIF) data. *International Journal of Wildland Fire* 30, 365–377. doi:10.1071/WF20162

Guo J, Wang J, Xu C, Song Y (2022) Modeling of spatial stratified heterogeneity. *GIScience & Remote Sensing* 59, 1660–1677. doi:10.1080/15481603.2022.2126375

Hao B, Xu X, Wu F, Tan L (2022) Long-Term Effects of Fire Severity and Climatic Factors on Post-Forest-Fire Vegetation Recovery. *Forests* 13, 883. doi:10.3390/f13060883

Hawe RG, Fuquay DM (1969) Remote sensing of lightning in forest fire research. *Remote Sensing of Environment* VI, 1193.

Hu L, Fan W, Ren H, Liu S, Cui Y, Zhao P (2018) Spatiotemporal Dynamics in Vegetation GPP over the Great Khingan Mountains Using GLASS Products from 1982 to 2015. *Remote Sensing* 10, 488. doi:10.3390/rs10030488

Hu T, Hu H, Li F, Zhao B, Wu S, Zhu G, Sun L (2019) Long-term effects of post-fire restoration types on nitrogen mineralisation in a Dahurian larch (*Larix gmelinii*) forest in boreal China. *Science of the Total Environment* 679, 237–247. doi:10.1016/j.scitotenv.2019.05.008

Hu Y, Xu E, Dong N, Tian G, Kim G, Song P, Ge S, Liu S (2022) Driving Mechanism of Habitat Quality at Different Grid-Scales in a Metropolitan City. *Forests* 13, 248. doi:10.3390/f13020248

Huang C, Goward SN, Masek JG, Thomas N, Zhu Z, Vogelmann JE (2010) An automated approach for reconstructing recent forest disturbance history using dense Landsat time series stacks. *Remote Sensing of Environment* 114, 183–198. doi:10.1016/j.rse.2009.08.017

Huo H, Sun C (2021) Spatiotemporal variation and influencing factors of vegetation dynamics based on Geodetector: A case study of the

northwestern Yunnan Plateau, China. *Ecological Indicators* **130**, 108005. doi:10.1016/j.ecolind.2021.108005

Jenks GF (1967) The data model concept in statistical mapping. *International Yearbook of Cartography* **7**, 186–190.

Jin S, Sader SA (2005) Comparison of time series tasseled cap wetness and the normalized difference moisture index in detecting forest disturbances. *Remote Sensing of Environment* **94**, 364–372. doi:10.1016/j.rse.2004.10.012

Jin Y, Randerson JT, Goetz SJ, Beck PSA, Loranty MM, Goulden ML (2012) The influence of burn severity on postfire vegetation recovery and albedo change during early succession in North American boreal forests. *Journal of Geophysical Research: Biogeosciences* **117**, G01036. doi:10.1029/2011JG001886

Jin X-Y, Jin H-J, Iwahana G, Marchenko SS, Luo D-L, Li X-Y, Liang S-H (2021) Impacts of climate-induced permafrost degradation on vegetation: A review. *Advances in Climate Change Research* **12**, 29–47. doi:10.1016/j.accre.2020.07.002

João T, João G, Bruno M, João H (2018) Indicator-based assessment of post-fire recovery dynamics using satellite NDVI time-series. *Ecological Indicators* **89**, 199–212. doi:10.1016/j.ecolind.2018.02.008

Kennedy RE, Yang Z, Cohen WB (2010) Detecting trends in forest disturbance and recovery using yearly Landsat time series: 1. LandTrendr — Temporal segmentation algorithms. *Remote Sensing of Environment* **114**, 2897–2910. doi:10.1016/j.rse.2010.07.008

Kennedy RE, Yang Z, Cohen WB, Pfaff E, Braaten J, Nelson P (2012) Spatial and temporal patterns of forest disturbance and regrowth within the area of the Northwest Forest Plan. *Remote Sensing of Environment* **122**, 117–133. doi:10.1016/j.rse.2011.09.024

Kennedy RE, Yang Z, Gorelick N, Braaten J, Cavalcante L, Cohen WB, Healey S (2018) Implementation of the LandTrendr Algorithm on Google Earth Engine. *Remote Sensing* **10**, 691. doi:10.3390/rs10050691

Key CH, Benson NC (2006) Landscape Assessment (LA): Sampling and Analysis Methods. In 'FIREMON: Fire Effects Monitoring and Inventory System' Gen. Tech. Rep. RMRS-GTR-164-CD. (Eds DC Lutes, RE Keane, JF Caratti, CH Key, NC Benson, S Sutherland, LJ Gangi) pp. LA-1–LA-55. (Ogden, UT: USDA Forest Service, Rocky Mountain Research Station) Available at https://www.fs.usda.gov/research/treesearch/24066

Kourtz PH (1968) Computers and Forest Fire Detection. *The Forestry Chronicle* **44**, 22–24. doi:10.5558/tfc44022-2

Lee H-J, Choi YE, Lee S-W (2018) Complex Relationships of the Effects of Topographic Characteristics and Susceptible Tree Cover on Burn Severity. *Sustainability* **10**, 295. doi:10.3390/su10020295

Li W, Jiang Y, Dong M, Du E, Wu F, Zhao S, Xu H (2021*a*) Species-specific growth-climate responses of Dahurian larch (*Larix gmelinii*) and Mongolian pine (*Pinus sylvestris* var. *mongolica*) in the Greater Khingan Range, northeast China. *Dendrochronologia* **65**, 125803. doi:10.1016/j.dendro.2020.125803

Li Y, Liu H, Zhu X, Yue Y, Xue J, Shi L (2021*b*) How permafrost degradation threatens boreal forest growth on its southern margin? *Science of the Total Environment* **762**, 143154. doi:10.1016/j.scitotenv.2020.143154

Liu Z (2016) Effects of climate and fire on short-term vegetation recovery in the boreal larch forests of Northeastern China. *Scientific Reports* **6**, 37572. doi:10.1038/srep37572

Liu L, Lu S (2020) Spatial-Temporal Landscape Dynamics in the Hulunbeir Forest-Steppe Ecotone. *Multifunctional Grasslands in a Changing World* **1**, 276.

Liu Y, Xie M, Liu J, Wang H, Chen B (2022) Vegetation Disturbance and Recovery Dynamics of Different Surface Mining Sites via the LandTrendr Algorithm: Case Study in Inner Mongolia, China. *Land* **11**, 856. doi:10.3390/land11060856

Luo W, Jasiewicz J, Stepinski T, Wang J, Xu C, Cang X (2016) Spatial association between dissection density and environmental factors over the entire conterminous United States. *Geophysical Research Letters* **43**, 692–700. doi:10.1002/2015GL066941

Marlon JR, Bartlein PJ, Carcaillet C, Gavin DG, Harrison SP, Higuera PE, Joos F, Power MJ, Prentice IC (2008) Climate and human influences on global biomass burning over the past two millennia. *Nature Geoscience* **1**, 697–702. doi:10.1038/ngeo313

Masson D, Knutti R (2011) Spatial-Scale Dependence of Climate Model Performance in the CMIP3 Ensemble. *Journal of Climate* **24**, 2680–2692. doi:10.1175/2011JCLI3513.1

McKetta CW (1969) Some effects of terrain on the application of airborne infrared line scanners to forest fire detection. Doctoral dissertation.

Meng R, Dennison PE, Huang C, Moritz MA, D'Antonio C (2015) Effects of fire severity and post-fire climate on short-term vegetation recovery of mixed-conifer and red fir forests in the Sierra Nevada Mountains of California. *Remote Sensing of Environment* **171**, 311–325. doi:10.1016/j.rse.2015.10.024

Pickell PD, Hermosilla T, Frazier RJ, Coops NC, Wulder MA (2016) Forest recovery trends derived from Landsat time series for North American boreal forests. *International Journal of Remote Sensing* **37**, 138–149. doi:10.1080/2150704X.2015.1126375

Powell SL, Cohen WB, Healey SP, Kennedy RE, Moisen GG, Pierce KB, Ohmann JL (2010) Quantification of live aboveground forest biomass dynamics with Landsat time-series and field inventory data: A comparison of empirical modeling approaches. *Remote Sensing of Environment* **114**, 1053–1068. doi:10.1016/j.rse.2009.12.018

Qiu J, Wang H, Shen W, Zhang Y, Su H, Li M (2021) Quantifying Forest Fire and Post-Fire Vegetation Recovery in the Daxin'anling Area of Northeastern China Using Landsat Time-Series Data and Machine Learning. *Remote Sensing* **13**, 792. doi:10.3390/rs13040792

Reygadas Langarica Y, Spera SA, Salisbury D, Galati V (2020) Mapping Forest Disturbances Across the Southwestern Amazon: Evaluation and Comparison of Optical Remote Sensing Algorithms. In 'American Geophysical Union, Fall Meeting 2020, abstract #GC103-0003'. Available at https://ui.adsabs.harvard.edu/abs/2020AGUFMGC1030003R/abstract

Rupp TS, Chapin III FS, Starfield AM (2000) Response of subarctic vegetation to transient climatic change on the Seward Peninsula in north-west Alaska. *Global Change Biology* **6**, 541–555. doi:10.1046/j.1365-2486.2000.00337.x

San-Miguel-Ayanz J, Moreno JM, Camia A (2013) Analysis of large fires in European Mediterranean landscapes: Lessons learned and perspectives. *Forest Ecology and Management* **294**, 11–22. doi:10.1016/j.foreco.2012.10.050

San-Miguel-Ayanz J, Durrant T, Boca R, Maianti P, Liberta G, Artes Vivancos T, Jacome Felix Oom D, Branco A, De Rigo D, Ferrari D, Pfeiffer H, Grecchi R, Nuitjen D (2020) Advance EFFIS report on forest fires in Europe, Middle East and North Africa 2019. EUR 30222 EN, Publications Office of the European Union, Luxembourg, JRC120692. Available at https://publications.jrc.ec.europa.eu/repository/handle/JRC120692

Seidl R, Thom D, Kautz M, Martin-Benito D, Peltoniemi M, Vacchiano G, Wild J, Ascoli D, Petr M, Honkaniemi J, Lexer MJ, Trotsiuk V, Mairota P, Svoboda M, Fabrika M, Nagel TA, Reyer CPO (2017) Forest disturbances under climate change. *Nature Climate Change* **7**, 395–402. doi:10.1038/nclimate3303

Shi L, Dech JP, Liu H, Zhao P, Bayin D, Zhou M (2019) Post-fire vegetation recovery at forest sites is affected by permafrost degradation in the Da Xing'an Mountains of northern China. *Journal of Vegetation Science* **30**, 940–949. doi:10.1111/jvs.12780

Siscawati M (1998) Underlying causes of deforestation and forest degradation in Indonesia: A case study on forest fire. In 'Proceedings of the IGES International Workshop on Forest Conservation Strategies for the Asia and Pacific Region' 21–23 July 1998. pp. 44–57 (Institute for Global Environmental Strategies) Available at https://www.iges.or.jp/en/publication_documents/pub/conferenceproceedings/en/744/1ws-7-mia.pdf

Song Y, Wright G, Wu P, Thatcher D, McHugh T, Li Q, Li SJ, Wang X (2018) Segment-Based Spatial Analysis for Assessing Road Infrastructure Performance Using Monitoring Observations and Remote Sensing Data. *Remote Sensing* **10**, 1696. doi:10.3390/rs10111696

Su Y, Li T, Cheng S, Wang X (2020) Spatial distribution exploration and driving factor identification for soil salinisation based on geodetector models in coastal area. *Ecological Engineering* **156**, 105961. doi:10.1016/j.ecoleng.2020.105961

Tadono T, Ishida H, Oda F, Naito S, Minakawa K, Iwamoto H (2014) Precise global DEM generation by ALOS PRISM. *ISPRS Annals of the Photogrammetry, Remote Sensing and Spatial Information Sciences* **II-4**, 71–76. doi:10.5194/isprsannals-II-4-71-2014

Takaku J, Tadono T, Tsutsui K (2014) Generation of High Resolution Global DSM from ALOS PRISM. *International Archives of the Photogrammetry, Remote Sensing and Spatial Information Sciences* **XL-4**, 243–248. doi:10.5194/isprsarchives-XL-4-243-2014

Takaku J, Tadono T, Tsutsui K, Ichikawa M (2016) Validation of "AW3D" global DSM generated from ALOS PRISM. *ISPRS Annals of the Photogrammetry, Remote Sensing and Spatial Information Sciences* **III-4**, 25–31. doi:10.5194/isprs-annals-III-4-25-2016

Tang H, Li Z, Zhu Z, Chen B, Zhang B, Xin X (2015) Variability and climate change trend in vegetation phenology of recent decades in the Greater Khingan Mountain area, Northeastern China. *Remote Sensing* **7**, 11914–11932. doi:10.3390/rs70911914

Thomas Ambadan J, Oja M, Gedalof ZE, Berg AA (2020) Satellite-Observed Soil Moisture as an Indicator of Wildfire Risk. *Remote Sensing* **12**, 1543. doi:10.3390/rs12101543

Tucker CJ (1979) Red and photographic infrared linear combinations for monitoring vegetation. *Remote Sensing of Environment* **8**, 127–150. doi:10.1016/0034-4257(79)90013-0

van Wagtendonk JW, Root RR, Key CH (2004) Comparison of AVIRIS and Landsat ETM+ detection capabilities for burn severity. *Remote Sensing of Environment* **92**, 397–408. doi:10.1016/j.rse.2003.12.015

Verbesselt J, Hyndman R, Newnham G, Culvenor D (2010) Detecting trend and seasonal changes in satellite image time series. *Remote Sensing of Environment* **114**, 106–115. doi:10.1016/j.rse.2009.08.014

Viana-Soto A, Aguado I, Martínez S (2017) Assessment of Post-Fire Vegetation Recovery Using Fire Severity and Geographical Data in the Mediterranean Region (Spain). *Environments* **4**, 90. doi:10.3390/environments4040090

Viana-Soto A, Aguado I, Salas J, García M (2020) Identifying Post-Fire Recovery Trajectories and Driving Factors Using Landsat Time Series in Fire-Prone Mediterranean Pine Forests. *Remote Sensing* **12**, 1499. doi:10.3390/rs12091499

Wang Z (2020) The Response of Soil Respiration to Wildfire Interference and Burned Area Management in the Permafrost Region of Da xing'an Mountains, Inner Mongolia (in Chinese). PhD thesis, Inner Mongolia Agricultural University.

Wang JF, Li XH, Christakos G, Liao YL, Zhang T, Gu X, Zheng XY (2010) Geographical detectors-based health risk assessment and its application in the neural tube defects study of the Heshun Region, China. *International Journal of Geographical Information Science* **24**, 107–127. doi:10.1080/13658810802443457

Wang J-F, Zhang T-L, Fu B-J (2016) A measure of spatial stratified heterogeneity. *Ecological Indicators* **67**, 250–256. doi:10.1016/j.ecolind.2016.02.052

Wang J, Wang C, Zang S (2017) Assessing re-composition of Xing'an larch in boreal forests after the 1987 fire, Northeast China. *Remote Sensing* **9**, 504. doi:10.3390/rs9050504

Wang S, Zhong R, Liu L, Zhang J (2021) Ecological Effect of Ecological Engineering Projects on Low-Temperature Forest Cover in Great Khingan Mountain, China. *International Journal of Environmental Research and Public Health* **18**, 10625. doi:10.3390/ijerph182010625

White J, Ryan K, Key C, Running S (1996) Remote Sensing of Forest Fire Severity and Vegetation Recovery. *International Journal of Wildland Fire* **6**, 125–136. doi:10.1071/WF9960125

Wittenberg L, van der Wal H, Keesstra S, Tessler N (2020) Post-fire management treatment effects on soil properties and burned area restoration in a wildland-urban interface, Haifa Fire case study. *Science of The Total Environment* **716**, 135190. doi:10.1016/j.scitotenv.2019.135190

Xiao X, Boles S, Liu J, Zhuang D, Liu M (2002) Characterization of forest types in Northeastern China, using multi-temporal SPOT-4 VEGETATION sensor data. *Remote Sensing of Environment* **82**, 335–348. doi:10.1016/S0034-4257(02)00051-2

Xu C, Wang J (2016) Geodetector. Available at http://www.geodetector.cn/

Xu Q, Dong Y, Wang Y, Yang R, Xu C (2018) Determinants and identification of the northern boundary of China's tropical zone. *Journal of Geographical Sciences* **28**, 31–45. doi:10.1007/s11442-018-1457-1

Yang J, Cooper DJ, Li Z, Song W, Zhang Y, Zhao B, Han S, Wang X (2020) Differences in tree and shrub growth responses to climate change in a boreal forest in China. *Dendrochronologia* **63**, 125744. doi:10.1016/j.dendro.2020.125744

Yang S, Lupascu M, Meel KS (2021) Predicting Forest Fire Using Remote Sensing Data And Machine Learning. *Proceedings of the AAAI Conference on Artificial Intelligence* **35**, 14983–14990. doi:10.1609/aaai.v35i17.17758

Yao Q, Brown PM, Liu S, Rocca ME, Trouet V, Zheng B, Chen H, Li Y, Liu D, Wang X (2017) Pacific-Atlantic Ocean influence on wildfires in northeast China (1774 to 2010). *Geophysical Research Letters* **44**, 1025–1033. doi:10.1002/2016GL071821

Ying H, Zhang H, Zhao J, Shan Y, Zhang Z, Guo X, Rihan W, Deng G (2020) Effects of spring and summer extreme climate events on the autumn phenology of different vegetation types of Inner Mongolia, China, from 1982 to 2015. *Ecological Indicators* **111**, 105974. doi:10.1016/j.ecolind.2019.105974

Yue Y, Liu H, Xue J, Li Y, Guo W (2020) Ecological indicators of near-surface permafrost habitat at the southern margin of the boreal forest in China. *Ecological Indicators* **108**, 105714. doi:10.1016/j.ecolind.2019.105714

Zhang Z, Wu Q, Xun X, Wang B, Wang X (2018) Climate change and the distribution of frozen soil in 1980–2010 in northern northeast China. *Quaternary International* **467**, 230–241. doi:10.1016/j.quaint.2018.01.015

Zhang Y, Li D, Liu L, Liang Z, Shen J, Wei F, Li S (2021) Spatiotemporal Characteristics of the Surface Urban Heat Island and Its Driving Factors Based on Local Climate Zones and Population in Beijing, China. *Atmosphere* **12**, 1271. doi:10.3390/atmos12101271

Zhao FR, Meng R, Huang C, Zhao M, Zhao FA, Gong P, Yu L, Zhu Z (2016) Long-Term Post-Disturbance Forest Recovery in the Greater Yellowstone Ecosystem Analyzed Using Landsat Time Series Stack. *Remote Sensing* **8**, 898. doi:10.3390/rs8110898

Zheng K, Tan L, Sun Y, Wu Y, Duan Z, Xu Y, Gao C (2021) Impacts of climate change and anthropogenic activities on vegetation change: Evidence from typical areas in China. *Ecological Indicators* **126**, 107648. doi:10.1016/j.ecolind.2021.107648

Zhu Z (2017) Change detection using landsat time series: A review of frequencies, preprocessing, algorithms, and applications. *ISPRS Journal of Photogrammetry and Remote Sensing* **130**, 370–384. doi:10.1016/j.isprsjprs.2017.06.013

Zhu Z, Woodcock CE, Olofsson P (2012) Continuous monitoring of forest disturbance using all available Landsat imagery. *Remote Sensing of Environment* **122**, 75–91. doi:10.1016/j.rse.2011.10.030

Zhu L, Meng J, Zhu L (2020) Applying Geodetector to disentangle the contributions of natural and anthropogenic factors to NDVI variations in the middle reaches of the Heihe River Basin. *Ecological Indicators* **117**, 106545. doi:10.1016/j.ecolind.2020.106545

Author affiliations
[A]Forestry College, Inner Mongolia Agricultural University, No. 275, East Xin Jian Street, Hohhot, 010011, China.
[B]Centre Eau Terre Environnement, Institut National de la Recherche Scientifique, Québec, Canada.